

# SCIENTIFIC REPORTS



OPEN

## High-fidelity self-assembly pathways for hydrogen-bonding molecular semiconductors

Xu Lin<sup>1</sup>, Mika Suzuki<sup>1</sup>, Marina Gushiken<sup>1</sup>, Mitsuaki Yamauchi<sup>1</sup>, Takashi Karatsu<sup>1</sup>, Takahiro Kizaki<sup>2</sup>, Yuki Tani<sup>2</sup>, Ken-ichi Nakayama<sup>3</sup>, Mitsuharu Suzuki<sup>4</sup>, Hiroko Yamada<sup>4</sup>, Takashi Kajitani<sup>5,6</sup>, Takanori Fukushima<sup>5</sup>, Yoshihiro Kikkawa<sup>7</sup> & Shiki Yagai<sup>1</sup>

Received: 16 August 2016  
Accepted: 18 January 2017  
Published: 22 February 2017

The design of molecular systems with high-fidelity self-assembly pathways that include several levels of hierarchy is of primary importance for the understanding of structure-function relationships, as well as for controlling the functionality of organic materials. Reported herein is a high-fidelity self-assembly system that comprises two hydrogen-bonding molecular semiconductors with regioisomerically attached short alkyl chains. Despite the availability of both discrete cyclic and polymeric linear hydrogen-bonding motifs, the two regioisomers select one of the two motifs in homogeneous solution as well as at the 2D-confined liquid-solid interface. This selectivity arises from the high directionality of the involved hydrogen-bonding interactions, which renders rerouting to other self-assembly pathways difficult. In thin films and in the bulk, the resulting hydrogen-bonded assemblies further organize into the expected columnar and lamellar higher-order architectures via solution processing. The contrasting organized structures of these regioisomers are reflected in their notably different miscibility with soluble fullerene derivatives in the solid state. Thus, electron donor-acceptor blend films deliver a distinctly different photovoltaic performance, despite their virtually identical intrinsic optoelectronic properties. Currently, we attribute this high-fidelity control via self-assembly pathways to the molecular design of these supramolecular semiconductors, which lacks structure-determining long aliphatic chains.

Precise control over the self-assembly pathway of supramolecular building blocks<sup>1,2</sup> with a  $\pi$ -conjugated core (henceforth: supramolecular  $\pi$ -building blocks) is crucial for the generation of specifically organized structures with desirable optoelectronic properties<sup>3</sup>. Due to the structural complexity in supramolecular  $\pi$ -building blocks that may favor specific conformations for a set of given conditions<sup>4–7</sup>, it still remains challenging to control their self-assembly pathways, which may include several levels of hierarchy from dilute solution to the bulk<sup>8,9</sup>. One of the structural elements that can lead to more complex pathways are long aliphatic chains, which endow the supramolecular  $\pi$ -building blocks with solubility and processability, as well as the resulting assemblies with softness<sup>10–12</sup>. These flexible units not only increase the kinetic stability of the assembled structures under specific conditions, but also influence thermodynamically stable structures during their transfer from solution to the bulk<sup>4,13–15</sup>. Moreover, a thermal treatment in the bulk may further affect the self-assembled structures by transferring the aliphatic chains into the molten state<sup>16,17</sup>.

In this context, the design of solution-processable supramolecular  $\pi$ -building blocks that do not contain long aliphatic chains should be promising not only from a practical perspective<sup>18–20</sup>, but also with regard to the high probability of generating the desired hierarchically organized architectures via high-fidelity

<sup>1</sup>Graduate School of Engineering, Chiba University, 1-33 Yayoi-cho, Inage-ku, Chiba 263-8522, Japan. <sup>2</sup>Graduate School of Science and Engineering, Yamagata University, 4-3-16 Jonan, Yonezawa, Yamagata 992-8510, Japan. <sup>3</sup>Graduate School of Engineering, Osaka University, 2-1 Yamadaoka, Suita, Osaka 565-0871, Japan. <sup>4</sup>Graduate School of Material Science, Nara Institute of Science and Technology (NAIST), 8916-5 Takayama-cho, Ikoma, Nara 630-0192, Japan. <sup>5</sup>Laboratory for Chemistry and Life Science, Institute of Innovative Research, Tokyo Institute of Technology, 4259 Nagatsuta, Midori-ku, Yokohama 226-8503, Japan. <sup>6</sup>RIKEN SPring-8 Center, 1-1-1 Kouto, Sayo, Hyogo 679-5148, Japan. <sup>7</sup>National Institute of Advanced Industrial Science and Technology (AIST), 1-1-1 Higashi, Tsukuba, Ibaraki 305-8562, Japan. Correspondence and requests for materials should be addressed to S.Y. (email: yagai@faculty.chiba-u.jp)

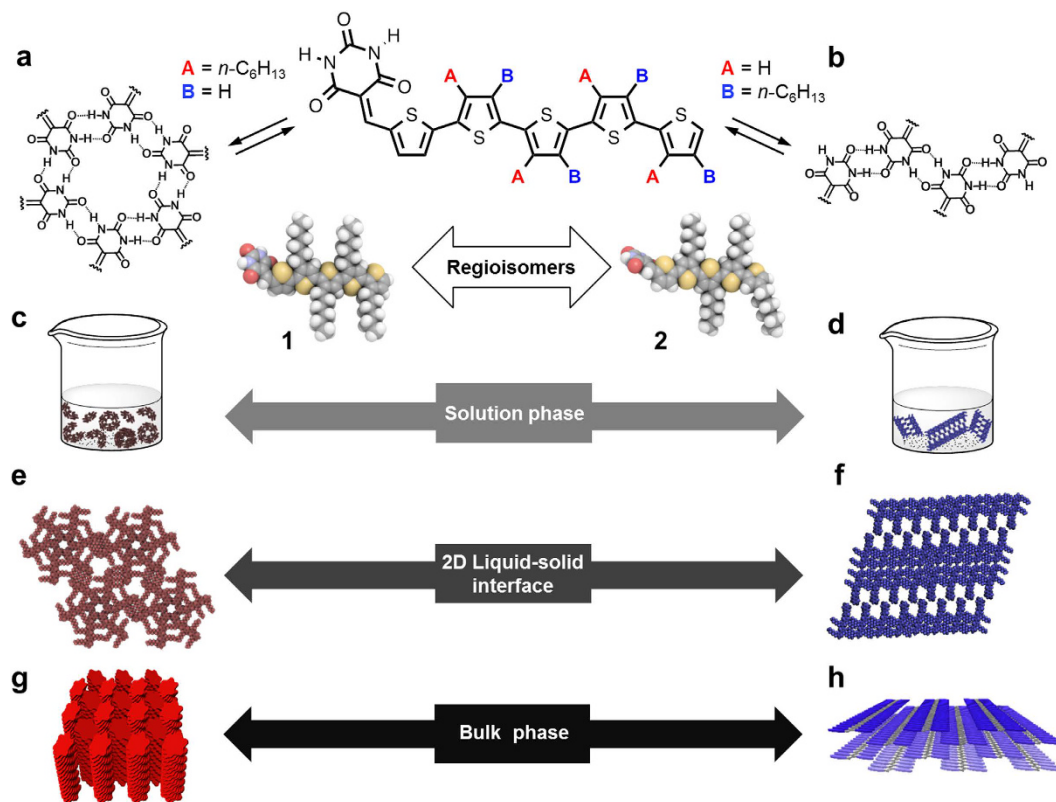


**Figure 1. Hierarchical self-assembly of **1** and **2** in different phases.** (a,b) Chemical structures and molecular models of hydrogen-bonding regioisomeric semiconductors **1** and **2** and their different hydrogen bonding motifs. (c–h) Schematic representation of the hierarchical organization of **1** and **2** in different phases.

self-assembly pathways. Such a design should be particularly effective for systems that are based on directional hydrogen-bonding interactions, where usually a drastic structural alteration is induced by the rearrangement of the hydrogen-bonding motif upon increasing the level of self-assembly hierarchy or by applying external stimuli<sup>21–24</sup>. Herein, we report high-fidelity self-assembly pathways of two hydrogen-bonding supramolecular oligothiophene  $\pi$ -building blocks<sup>25–28</sup> with regioisomerically attached short alkyl side chains. As the short alkyl chains in these molecules are grafted onto the  $\pi$ -conjugated backbone, they are embedded within the supramolecular structure, which endows the resulting supramolecular assemblies with good solubility. Such regioisomerically attached alkyl chains also give rise to different molecular conformations due to steric demand, which results in a thermodynamic preference for either cyclic or linear hydrogen-bonding motifs. Remarkably, the supramolecular structures formed in solution are preserved upon removal of the solvent, thus yielding predictably organized solid supramolecular architectures. These results demonstrate that control over high-fidelity pathways may substantially impact supramolecular architectures in the solid state, especially upon co-organization with structurally different molecular components for applications in photovoltaic devices.

## Results and Discussion

**Regioisomers.** Regioisomeric quinquethiophenes **1**<sup>20</sup> and **2** with barbituric acid group are purple dyes that exhibit an absorption maximum at  $\sim 550$  nm in  $\text{CHCl}_3$  (Fig. 1a, see Supplementary Fig. S11). Despite similarity in their molecular structures, **1** is significantly more soluble in  $\text{CHCl}_3$  (400 mM, *i.e.*  $\sim 355$  mg/mL) than **2** (100 mM, *i.e.*  $\sim 89$  mg/mL). Furthermore, the melting point (m.p.) of **1** (145 °C, 2nd heating scan in a differential scanning calorimetry (DSC) measurement) is lower than that of **2** (165 °C, 2nd heating scan in a DSC measurement). We thus expected **1** and **2** to self-organize in different supramolecular structures via self-complementary hydrogen bonds.

**Self-assembly in solution.** Because of the absence of reasonable multicomponent self-assembly systems that provide both cyclic and polymeric hydrogen-bonded aggregates soluble without forming higher-order assemblies, the structural preference for these competing hydrogen-bonded motifs have been mainly studied based on solid-state packing structures provided by X-ray crystallography<sup>29</sup> or theoretical approaches<sup>30</sup>. Following vapor pressure osmometry (VPO)<sup>31–33</sup> and nuclear magnetic resonance (NMR) studies of **1** and **2** in chloroform however reveal such a structural preference could occur in equilibrated solution state.

VPO measurements of chloroform solutions of **1** and **2** at substrate concentrations ( $c_{\text{subs}}$ ) from 10 to 100 mM displayed markedly different concentration-dependence on aggregation (see Supplementary Fig. S12). For **1**, the average aggregation number  $N = c_{\text{subs}}/c_{\text{collig}}$ , wherein  $c_{\text{collig}}$  is the colligative concentration measured by VPO,

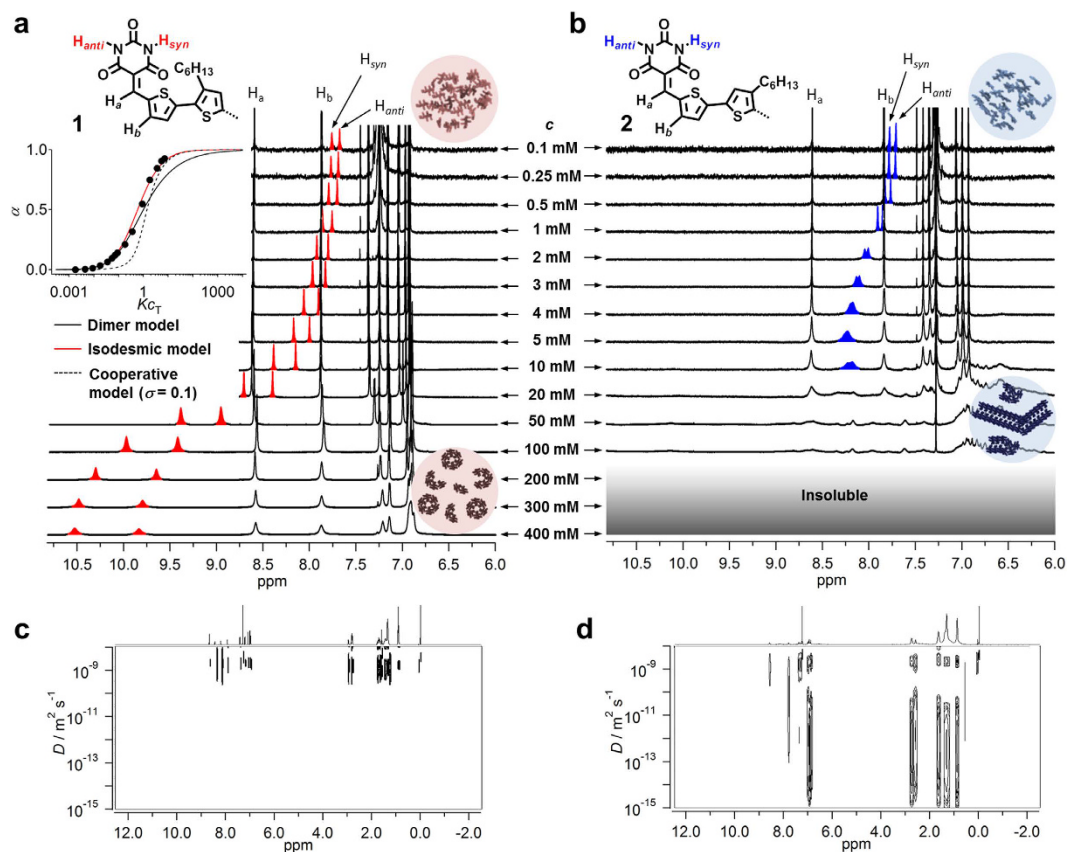


**Figure 2.** NMR studies of **1** and **2**. (a) Concentration-dependent  $^1\text{H}$  NMR spectra of **1** ( $c = 0.1\text{--}400$  mM) in  $\text{CDCl}_3$  at  $25^\circ\text{C}$ . Inset: fraction of aggregated molecules ( $\alpha$ ) calculated from the chemical shift changes of the NH protons of **1** as a function of  $Kc_T$  ( $c_T$ , total concentration of the molecules). Black solid, red solid and black dashed curves represent simulated curves according to dimer, isodesmic, and cooperative ( $\sigma = K_2/K = 0.1$ ) models, respectively. (b) Concentration-dependent  $^1\text{H}$  NMR spectra of **2** ( $c = 0.1\text{--}100$  mM) in  $\text{CDCl}_3$  at  $25^\circ\text{C}$ . (c,d) DOSY NMR spectra of **1** ( $c = 10$  mM) (c) and **2** ( $c = 10$  mM) (d) in  $\text{CDCl}_3$ .  $D$  = diffusion coefficient.

increased from 1.3 to 2.1 upon increasing concentration from 10 mM to 100 mM. Though the results are indicative of the formation of dimers, the selective formation of dimers was clearly discarded on account of the following concentration-dependent NMR study that illustrate the formation of larger oligomers including cyclic hexamers (rosettes). Furthermore, the presence of residual monomers (ca. 20%) in the monomer-aggregate equilibrium could seriously influence  $c_{\text{colli}}$ , leading to this underestimation of  $N^{32}$ . On the contrary, **2** exhibited a linear increase of  $N$  with increasing concentration, and  $N$  reached 9.9 for  $c = 100$  mM. This tractable concentration-dependence of  $N$  is in good agreement with the formation of open-ended oligomers. For both compounds, VPO measurements for  $c > 100$  mM were hampered by the formation of films at the surface of solution droplets, which gradually decreased the instrument response.

Concentration-dependent  $^1\text{H}$  NMR spectra of  $\text{CDCl}_3$  solutions of the regioisomers further demonstrate preferential formation of distinct hydrogen-bonded assemblies (Fig. 2a,b). At submillimolar concentrations, both the regioisomers displayed sharp signals in the range of 7.67–7.83 ppm for the NH protons of the barbituric acid moiety ( $\text{H}_{\text{syn}}$  and  $\text{H}_{\text{anti}}$ )<sup>34</sup>, indicating the absence of hydrogen bonding interactions. Upon increasing the concentration to  $c = 1$  mM, these two NH signals experienced a gradual downfield shift. For **1**, the downfield shift continued upon increasing the concentration up to  $c = 400$  mM, and the difference in chemical shift for the two NH signals increased with increasing concentration (Fig. 2a). In contrast, the signals of the aromatic protons  $\text{H}_a$  and  $\text{H}_b$  remained, while broadening, almost constant as a function of increasing concentration, suggesting that **1** forms hydrogen-bonded oligomeric species in  $\text{CDCl}_3$ . The observed large difference between the chemical shifts of  $\text{H}_{\text{syn}}$  and  $\text{H}_{\text{anti}}$  at  $c > 200$  mM (e.g.  $\Delta\delta = 0.69$  ppm at  $c = 400$  mM) relative to the monomeric state ( $\Delta\delta = 0.08$  ppm at  $c = 0.1$  mM) illustrates that these protons are subjected to distinct deshielding effects from neighboring molecules. This finding demonstrates that hydrogen-bonding between **1** molecules occurs with a specific configuration. Hence, the formation of screw-shaped hydrogen-bonded rosettes, which is confirmed by the following STM study, and the corresponding intermediate oligomers ( $c \ll 400$  mM) are strongly suggested. Plotting the mole fraction of aggregated molecules  $\alpha$ , obtained from  $\alpha = [\delta - \delta(0.1 \text{ mM})]/[\delta(400 \text{ mM}) - \delta(0.1 \text{ mM})]$ , against the concentration revealed a sigmoidal transition from the monomeric to the aggregated state. This transition could be fitted well using the equal  $K$  (isodesmic) model<sup>35</sup>, but deviated substantially from both the dimer model<sup>36</sup> as well as the cooperative model<sup>37,38</sup> (inset, Fig. 2a). The apparent isodesmic association constant ( $K_{\text{iso}}$ ) in  $\text{CDCl}_3$  was estimated as  $K_{\text{iso}} = 18 \text{ M}^{-1}$ . The variable-temperature  $^1\text{H}$  NMR measurements ( $20\text{--}60^\circ\text{C}$ ) at  $c = 20$  mM showed a

change of  $\alpha$  (0.34–0.14) as a function of temperature, which can be fitted with the isodesmic model with an apparent association constant ( $K_{\text{iso}}$ ) of  $15 \text{ M}^{-1}$  (see Supplementary Fig. S13a)<sup>37</sup>. Assuming the formation of hexameric rosettes according to the isodesmic process given in the Supplementary Scheme S1 furnished the  $K_{\text{rosette}} (=K_{\text{iso}}^5) = 1.89 \times 10^6 \text{ M}^{-5}$  based on the concentration-dependent data<sup>39</sup>.

Compound **2** exhibited a decidedly different behavior in such a concentration-dependent <sup>1</sup>H NMR study (Fig. 2b). The signals of  $\text{H}_{\text{syn}}$  and  $\text{H}_{\text{anti}}$  shifted downfield up to  $c = 1 \text{ mM}$ , but with diminishing the difference between the two ( $\Delta\delta = 0.07 \text{ ppm}$  at  $c = 0.1 \text{ mM}$ ,  $\Delta\delta = 0.05 \text{ ppm}$  at  $c = 1 \text{ mM}$ ). This trend is very contrastive to that of **1**, and already at this concentration, different oligomeric species seem to be formed from **2**. Thus, it is evident that the effective molarity (EM) of **2** in hydrogen-bond-directed macrocyclization is very low ( $[\text{2}]_{\text{EM}} \approx 1 \text{ mM}$ ) compared to that of **1** ( $[\text{1}]_{\text{EM}} \gg 100 \text{ mM}$ ). With further increasing concentration, the downfield shift of the two NH signals leveled off at approximately  $c = 4 \text{ mM}$ , where the two signals coalesced. This change is very contrastive to that observed for **1**, and implies that hydrogen-bonding between **2** molecules occurs in non-specific configuration even at this concentration. Further increasing the concentration ( $c > 10 \text{ mM}$ ) caused broadening of all sharp signals with emergence of new complex signals at 6.0–7.0 ppm. These signal patterns unequivocally indicate absence of specific supramolecular species, and reflect the coexistence of diverse polymeric assemblies, the interconversion of which is too slow on the NMR time scale to produce average signals. In a variable-temperature measurement (20–60 °C) at  $c = 20 \text{ mM}$ , only the sharpening of proton signals was induced by the disruption of polymeric assemblies (see Supplementary Fig. S13b). All of these observations corroborate the formation of open-ended polydispersed polymeric assemblies.

Diffusion-ordered spectroscopy (DOSY) NMR experiments further provided strong evidence for the formation of different assembly types for **1** and **2** in  $\text{CDCl}_3$ . At  $c = 1 \text{ mM}$ , similar average diffusion coefficients were observed for both compounds (**1**:  $D_{\text{ave}} = 1.32 \times 10^{-9} \text{ m}^2 \text{ s}^{-1}$ , **2**:  $1.47 \times 10^{-9} \text{ m}^2 \text{ s}^{-1}$ ) (see Supplementary Fig. S14). These values are comparable with those of non-aggregative *N,N'*-dimethyl derivatives **1-Me** ( $1.48 \times 10^{-9} \text{ m}^2 \text{ s}^{-1}$ ) and **2-Me** ( $1.75 \times 10^{-9} \text{ m}^2 \text{ s}^{-1}$ ) measured at  $c = 10 \text{ mM}$  (see Supplementary Fig. S15). Upon increasing the concentration to  $c = 10 \text{ mM}$ , the  $D_{\text{ave}}$  value for **1** changed only marginally ( $1.32 \times 10^{-9} \text{ m}^2 \text{ s}^{-1}$ ; Fig. 2c), due to the presence of a low fraction of aggregated molecules ( $\alpha = 0.23$ ; see Supplementary Fig. S12) at this concentration. Unfortunately, DOSY measurements at higher concentrations ( $c > 100 \text{ mM}$ ;  $\alpha = 0.81$ ) were hampered by severe broadening of the DOSY signals, most likely due to the high concentrations of the solute (5.9 wt%). In striking contrast, a solution of **2** at  $c = 10 \text{ mM}$  provided broadly distributed diffusion coefficients ( $D = 4 \times 10^{-11} - 1 \times 10^{-15} \text{ m}^2 \text{ s}^{-1}$ ), resulting in a  $D_{\text{ave}}$  value of  $4.2 \times 10^{-13} \text{ m}^2 \text{ s}^{-1}$  (Fig. 2d), which suggests the presence of large polydispersed assemblies in addition to monomers. Although the exact aggregation number could not be estimated for **1**, the contrastive DOSY NMR results clearly demonstrate distinct inherent aggregation propensity of the two regioisomers.

**Self-Assembly in a 2D-confined space.** Given the contrastive results in the solution-state studies, we attempted to directly visualize hydrogen-bonded aggregates at the liquid–solid interface by means of scanning tunneling microscopy (STM). According to the previous observations<sup>20,40,41</sup>, our hydrogen-bonded assemblies could be chiral at the solid–liquid interface<sup>42,43</sup>. The formation of two enantiomeric hydrogen-bonded assemblies from achiral components on achiral surface may decrease packing efficiency, which in turn decrease the resolution of the STM imaging. We thus used (*S*)- and (*R*)-limonene as the chiral liquid phase<sup>44,45</sup> in the STM analysis, with the expectation that enantiomerically enriched supramolecular packing through surface confined process (Fig. 3a)<sup>46</sup>.

Figure 3 displays typical STM images of **1** and **2** at the (*S*)- or (*R*)-limonene–HOPG interface. For **1**, closely packed screw-shaped hexameric rosettes that rotate exclusively clockwise (CW) or counterclockwise (CCW) were observed for (*S*)- or (*R*)-limonene, respectively (Fig. 3b,g). The observed unit cell parameters ( $\alpha = 4.9 \pm 0.2 \text{ nm}$ ,  $\beta = 4.8 \pm 0.2 \text{ nm}$ , and  $\gamma = 62 \pm 3^\circ$ ) indicated the formation of a pseudohexagonal lattice, which could be reasonably reproduced by molecular modeling (Fig. 3c,f). In sharp contrast, **2** showed lamellar arrangements of the building blocks (Fig. 3d,i). The results of complementary molecular modeling calculations showed that the interlayer spacing L1 (4.6 nm) and the intermolecular distance L2 (1.4 nm) estimated from STM images agree very well with the longer length of the hydrogen-bonded dimeric unit and the distance between the neighbouring dimeric units, respectively (Fig. 3e,h). Exclusive CCW or CW orientations of the dimeric units with respect to the normal of the lamellae were observed for the (*S*)- and (*R*)-limonene–HOPG interfaces, respectively (inset, Fig. 3d,i)<sup>42</sup>. Thus, **2** exclusively forms infinite hydrogen-bonded tape-like molecular arrays, as observed for a barbituric acid-functionalized merocyanine<sup>47</sup> and a fullerene derivative<sup>48</sup>. These strong preference of the hydrogen-bonded patterns at the liquid–solid interface is concentration-independent ( $c = 0.005$ – $0.1 \text{ mM}$ ) under the applied experimental conditions<sup>49</sup>, and also is not observed for the 2D molecular packing of regioisomeric *N,N'*-dimethylated derivatives **1-Me** and **2-Me**, which lack the hydrogen-bonding arising from the barbituric acid moieties (see Supplementary Fig. S16). Hence, it can be concluded that the observed 2D assembly of **1** and **2** is supported by hydrogen-bonding interactions and the two regioisomers favor entirely different hydrogen-bonded molecular arrays not only solution phase but also at the solid–liquid interface.

**Mechanism.** The preferential formation of the specific hydrogen-bonded motif of **1** and **2** in the 2D-confined space is partially influenced by the kinetic stability of the 2D-packed hydrogen-bonded molecular arrays<sup>50</sup>. However, upon considering the obtained VPO and NMR results, it can be concluded that aggregation driven by such specific hydrogen-bonding motif occur under equilibrium conditions as a result of their thermodynamic preference arising from the regioisomerically attached side chains. In melamine and barbiturate/cyanurate ditopic bicomponent systems, the mechanism for the structural preference between cyclic rosettes and open-ended polymeric motifs has been the subject of controversial discussions<sup>29,30,51</sup>. On the basis of intricate theoretical simulations for the equilibrium between cyclic and other open-ended oligomers in the bicomponent mixtures, Reinhoudt and coworkers concluded that the steric hindrance, which only affects the internal energy

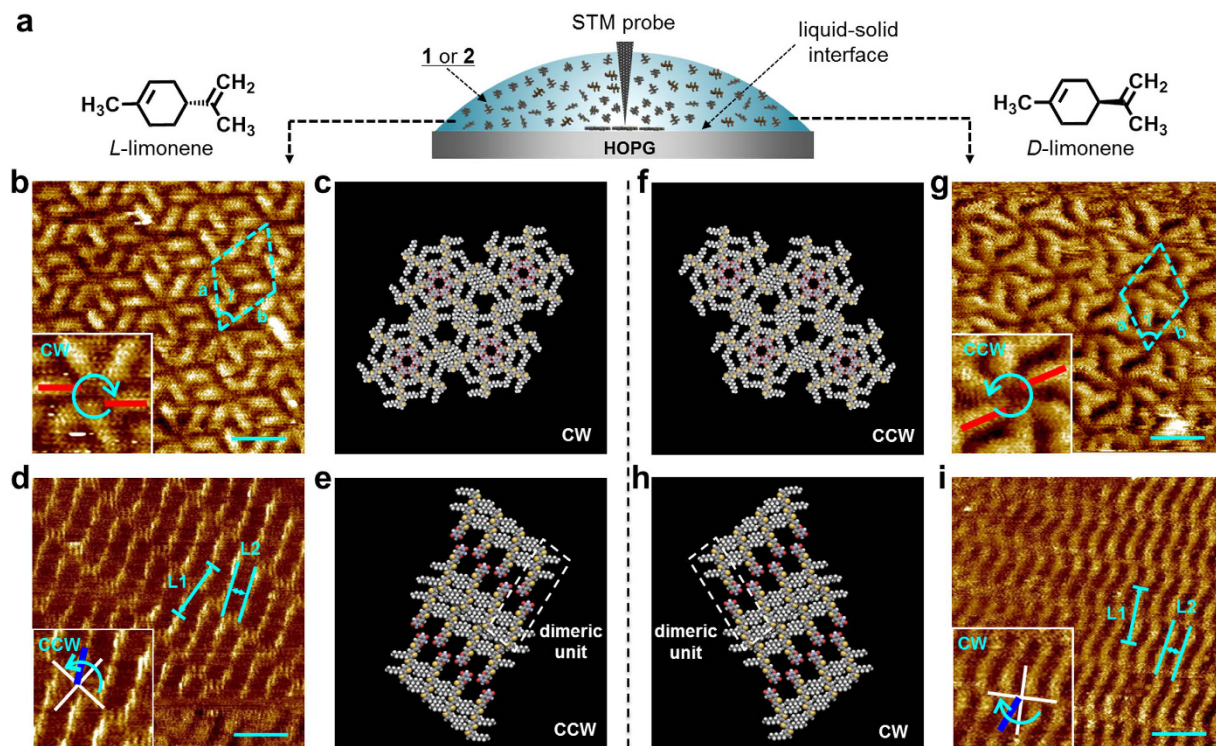


**Figure 3.** STM studies of **1** and **2**. (a) Schematic diagram of STM measurements on chiral liquid-solid interface. (b,d) STM images of **1** (b) and **2** (d) at the (*S*)-limonene–HOPG interface with the following tunneling conditions:  $I = 1.5$  pA,  $V = -1000$  mV;  $I = 2.0$  pA,  $V = -1000$  mV. Concentration of solution is 0.005 mM for both cases. Scale bar, 4 nm. (g,i) STM images of **1** (g) and **2** (i) at (*R*)-limonene–HOPG interface with the following tunneling conditions:  $I = 1.5$  pA,  $V = -1000$  mV;  $I = 3.0$  pA,  $V = -900$  mV. Concentration of solution is 0.006 mM for both cases. Scale bar, 4 nm. (c,e,f,h) Packing models of CW rosettes of **1** (c), CCW tapes of **2** (e), CCW rosettes of **1** (f) and CW tapes of **2** (h).

of the open-ended assemblies, should hardly affect the cyclic rosette/open-ended oligomers ratio<sup>30</sup>. This behavior should be attributed to the buffering effect of repulsive interactions in a large number of open-ended species - a notion that was supported by the observation of broad signals in the <sup>1</sup>H NMR spectra of **2** for  $c > 10$  mM. In contrast, they proposed on the basis of a molecular modeling study, that the cyclic rosette/open-ended oligomers ratio should be very sensitive to steric parameters, which directly affect the internal energy of the rosettes.

Considering these results, we carried out molecular mechanics calculations on the rosettes as well as on monomers **1** and **2** (Supplementary Methods). Although the energy minimization did not show an appreciable difference between the stabilization energy of the regioisomers upon rosette formation, we observed a significant structural difference between these rosettes (Fig. 4a,b). In rosettes of **1**, all hexyl chains are arranged in the rosette plane, whereas in rosettes of **2**, they are aligned in perpendicular direction with respect to the rosette plane. This structural difference may facilitate van der Waals interactions between neighboring molecules within rosettes and their oligomeric intermediates of **1**, and thus induce stronger thermodynamic preference toward rosette formation for **1** compared to **2**. In the absence of such interactions, the formation of competing tape-like hydrogen-bonded species might prevail as experimentally observed for **2**.

The energy minimization of monomeric **1** and **2** furthermore revealed that the specific orientation of the hexyl chains in the rosettes is an intrinsic structural property of the monomers. In both regioisomers, the barbituric acid plane and the neighboring thiophene plane (*T1*) comprise a dihedral angle of 52–53°, which arises from the steric repulsion between one of the C=O groups of the barbituric acid and *T1* (Fig. 4c,d). In **1**, the adjacent thiophene plane (*T2*) is further twisted, including a dihedral angle of 23° between *T1* and *T2*, which arises from the steric demand of the 3-hexyl group of *T2* in order to counterbalance the twisting between the barbituric acid and *T1*. In contrast, the *T1* and *T2* planes in **2** are almost coplanar (dihedral angle = 0.8°) due to the absence of a hexyl group at the 3-position of *T2*. Hence, it is the twisting between the barbituric acid and *T1* that is predominantly responsible for the molecular shape of **2** observed in its rosette architecture. Accordingly, this subtle conformational difference in the molecular structures, induced by the position of the side chains, should control the initial self-assembly pathways via directional hydrogen bonds.

**Self-organization through solution processing.** The self-organized structures of **1** and **2** via the formation of the previously discussed hydrogen-bonded assemblies were investigated by powder X-ray diffraction (PXRD) measurements on bulk samples of **1** and **2**, which were obtained from solvent evaporation of their CHCl<sub>3</sub> solutions ( $c = 5$  mM). The bulk sample of **1** showed explicit diffraction peaks with *d*-spacings which

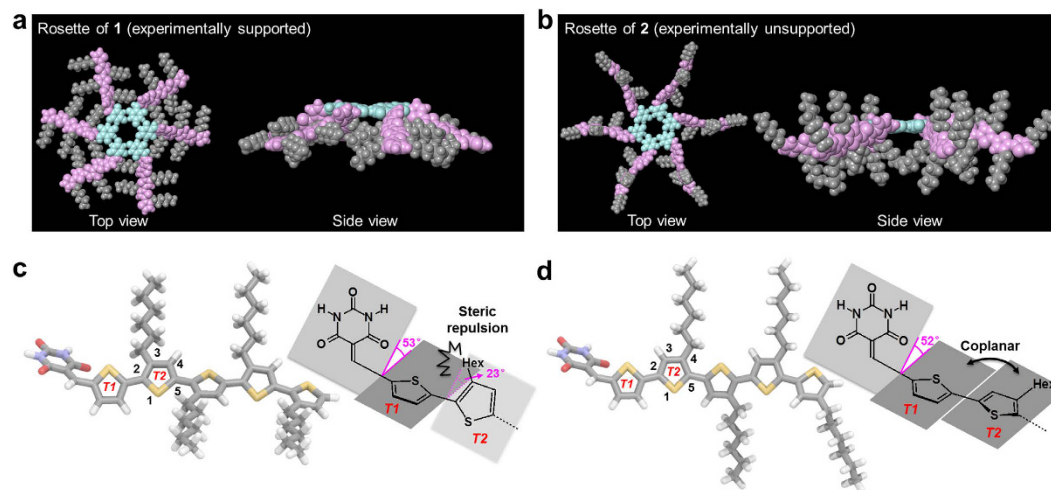


**Figure 4. Molecular modeling of 1 and 2.** (a–d) Geometry-optimized structures of hexameric rosettes (a,b) and monomers (c,d) of 1 (a,c) and 2 (b,d). The molecular modeled structures are shown in vertical (left) and perpendicular (right) direction with respect to the rosette plane. Barbituric acid, oligothiophene, and alkyl chain moieties are colored in light blue, purple, and gray, respectively. The twisting between the barbituric acid, T1, and T2 planes in the monomer structures is shown by a schematic cartoon.

can be assigned to the diffractions from the (110), (200), (210), (220), (001), (400), (420), and (421) planes of a 3D lattice (Fig. 5a). These results suggest that cyclic rosettes of **1** form a rectangular 2D lattice (space group:  $P2_1/a$ , lattice parameters:  $a = 4.9$  nm,  $b = 4.3$  nm) in the  $ab$  plane, which is complemented by the formation of one-dimensional columns along the  $c$  axis, obtained from the stacking of these rosettes with a periodic length of 1.4 nm (Fig. 5b,c)<sup>52–55</sup>. This structural periodicity might correspond to a helical pitch arising from helical stacking of the rosettes. Several diffraction peaks that could be attributed to the columnar stacked molecules were observed in the wide-angle region ( $q > 15$  nm<sup>-1</sup>).

The PXRD pattern of the bulk sample of **2** displayed seven peaks in the small-angle region (Fig. 5d), which could not be indexed considering usual columnar assembling motifs. Here, two sets of diffraction peaks ( $d$ -spacing of 3.44 and 1.72, as well as 1.42 and 0.71 nm) represent two different structural elements of periodicity (3.4 and 1.4 nm). Considering the presence of an additional diffraction peak with a  $d$ -spacing of 1.31 nm, these five peaks should be assigned, in order of decreasing  $d$ -spacing, to the diffractions from the (100), (200), (010), (020), and (110) planes of a 2D rectangular lattice (space group:  $P2m$ , lattice parameters:  $a = 3.4$  nm,  $b = 1.4$  nm). Given that the diffraction peak with a  $d$ -spacing of 0.96 nm should be attributed to a structural periodicity element along the  $c$  axis, the peak with a  $d$ -spacing of 0.57 nm should be attributed to the diffraction from the (021) plane. In light of the result from the aforementioned STM study, we would like to propose the following structure for self-organized **2** in the bulk. The lattice parameter  $b$  (1.4 nm) could feasibly be ascribed to the intermolecular distance L2 between dimeric units (Fig. 3d), suggesting that tape-like hydrogen-bonded supramolecular chains form along the  $b$ -axis (Fig. 5f). Conversely, the lattice parameter  $a$  (3.4 nm) is shorter than the width L1 (4.6 nm) of the supramolecular chains (Fig. 3d). Presumably, the supramolecular chains are packed in a slipped brick-like motif, where the oligothiophene units interdigitate each other upon stacking in direction of the  $c$ -axis (Fig. 5e,f). Similar to the case of **1**, several diffraction peaks were observed in the wide-angle region ( $q > 15$  nm<sup>-1</sup>), most likely arising from stacked oligothiophene units.

**Co-organization with fullerene semiconductor.** The distinct self-assembly pathways of **1** and **2** evolving through solvent evaporation were also manifested in a critical difference regarding their bulk-heterojunction (BHJ) structures with the ball-shaped molecular semiconductor [6,6]-phenyl-C<sub>61</sub>-butyric acid methyl ester (PC<sub>61</sub>BM)<sup>56,57</sup>. To obtain insight into the phase separation in BHJ structures, we studied thin films of individual semiconductors as well as their 1:1 (w/w) blends with PC<sub>61</sub>BM (denoted as **1**:PC<sub>61</sub>BM and **2**:PC<sub>61</sub>BM), which are prepared by spin-coating respective homogeneous CHCl<sub>3</sub> solutions. In differential scanning calorimetry (DSC), **1** exhibited on heating a sharp endothermic peak at 163 °C with an enthalpy change ( $\Delta H$ ) of 24.3 kJ/mol, which was ascribed to a melting transition (see Supplementary Fig. S17a, broken curve). In contrast, the thermogram of **1**:PC<sub>61</sub>BM displayed during the first heating scan merely a relatively undefined endothermic feature in the range of 107–150 °C ( $\Delta H = 14.9$  kJ/mol) (see Supplementary Fig. S17a, solid curve). The apparent significant discrepancy between the phase transitions of **1** and **1**:PC<sub>61</sub>BM implies that PC<sub>61</sub>BM hampers the self-organization of **1** upon evaporation of the solvent. Contrastingly, the DSC thermograms of **2** and **2**:PC<sub>61</sub>BM did not show such a significant difference, and both showed a sharp endothermic peak around 170 °C ascribed to a melting transition (see Supplementary Fig. S17b). We assume that the negligible impact of PC<sub>61</sub>BM on the organization of **2** reflect the occurrence of a macroscopic phase separation due to a morphological mismatch between the assemblies of **2** and PC<sub>61</sub>BM.

AFM images of the surface of the thin film of **1** showed particulate nanostructures (see Supplementary Fig. S18a). Thermal annealing of this film at 80 °C resulted in a directional elongation of particles up to the length of ~100 nm

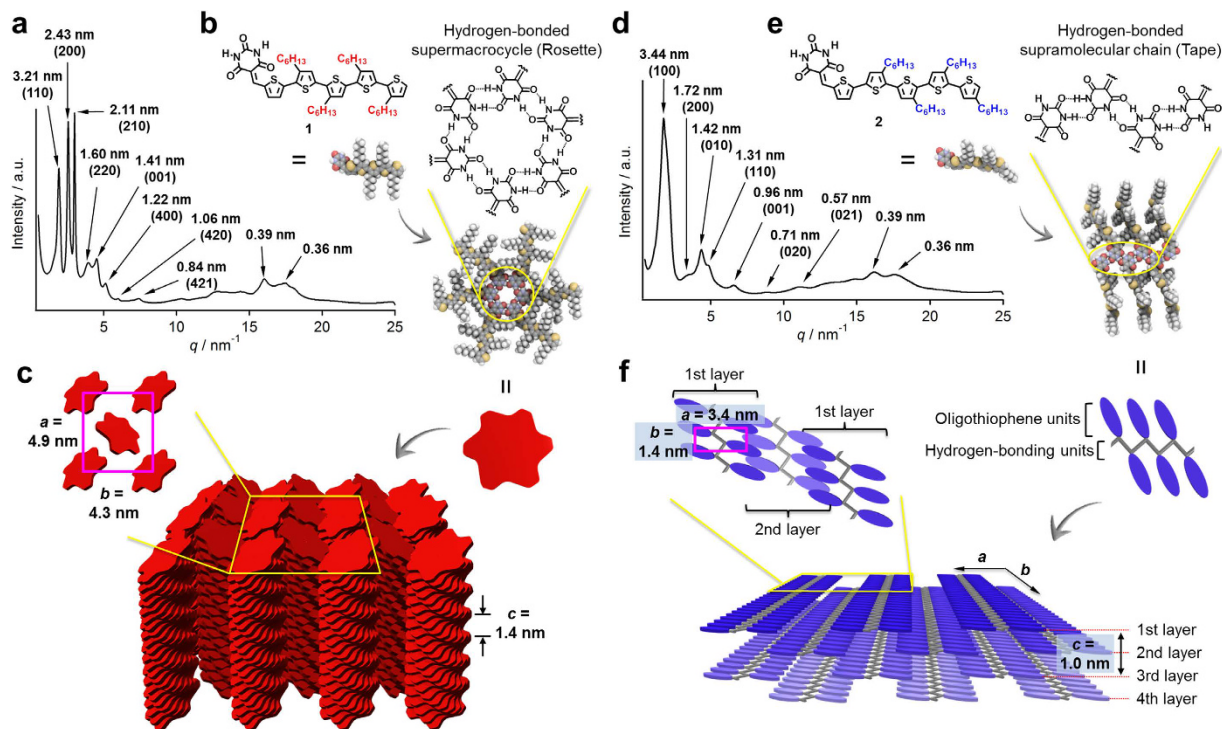


**Figure 5.** Self-organized structures of **1** and **2** in the bulk. (a,d) PXRD patterns of bulk samples of **1** (a) and **2** (d) at 25 °C in a glass capillary (diameter: 1.0 mm). Values in parenthesis denote Miller indices. (b,e) Molecular models of rosettes of **1** (b) and tapes of **2** (e). (c,f) Schematic representations of a proposed packing structures of **1** (c) and **2** (f) with lattice parameters. In (c), only left-handed helical columns are used to show the packing structure. As **1** does not contain a chiral center, both left- and right-handed helical columns should be formed.

(see Supplementary Fig. S18b). The grazing incidence X-ray diffraction (GI-XRD) image of the film displayed only a wide diffraction circle with a  $d$ -spacing of  $\sim 3.4$  nm (see Supplementary Fig. S18c), corresponding to the diffraction from the (110) plane of the rectangular lattice that was observed in the PXRD analysis of the bulk sample of **1** (Fig. 5a). Thermal annealing merely narrowed the width of this diffraction circle. For the thin film of **1**:PC<sub>61</sub>BM, a granularly nanostructured surface was observed by AFM similarly to that of **1** (Fig. 6a), suggesting the absence of any macroscopic phase separation between the two materials (Fig. 6e). Interestingly, thermal annealing of this blend film at 80 °C resulted in the horizontal growth of well-defined nanorods with a uniform diameter ( $\sim 20$  nm) and a length up to  $\sim 200$  nm (Fig. 6b). In line with the nanostructure change on the surface, the GI-XRD analysis of the thin film of **1**:PC<sub>61</sub>BM revealed a significant reorganization upon thermal annealing. The as-prepared blend film did not show any diffraction circle (see Supplementary Fig. S19c), corroborating the notion that PC<sub>61</sub>BM hampers the self-organization of **1**. However, the GI-XRD image after the thermal annealing featured a clear diffraction spot with a  $d$ -spacing of 2.5 nm that corresponds to the diffraction from the (200) plane of the rectangular lattice (Fig. 5a) in the meridional direction (see Supplementary Fig. S19d). Thus, the 2D rectangular lattice composed of rosette columns of **1** developed parallelly to the substrate in the presence of PC<sub>61</sub>BM upon thermal annealing, where the  $a$ -axis (Fig. 5c) is aligned vertically with respect to the substrate surface. Combined with the horizontal growth of the nanorods shown by AFM, the elongation of nanorods is driven by the stacking of rosettes along to the  $c$ -axis (Fig. 6f).

AFM images of a thin film of **2** showed a pronounced striped texture prior to thermal annealing (see Supplementary Fig. S20a), which developed into a clearer finger-print pattern posterior to thermal annealing at 80 °C (see Supplementary Fig. S20b). The pattern revealed a periodicity of  $\sim 4.7$  nm, which is commensurate with the width of the tape-like assemblies (Fig. 3d). The GI-XRD image of the as-prepared film of **2** displayed only a weak diffraction circle with a  $d$ -spacing of 3.6 nm (see Supplementary Fig. S20c), which should correspond to the diffraction from the (100) plane of the rectangular lattice observed for **2** in the bulk (Fig. 5d). Consistent with the AFM results, thermal annealing resulted in an increase of the structural order, as evident from the intensified XRD diffraction posterior to annealing (see Supplementary Fig. S20d). However, the extended lamellar organization **2** caused a significant phase-separation upon mixing with PC<sub>61</sub>BM, as shown by AFM images of the **2**:PC<sub>61</sub>BM film that feature submicrometer-sized grains of PC<sub>61</sub>BM (Fig. 6c,g). This phase-separation feature remained present, even after thermal annealing (Fig. 6d,h). As previously discussed, **1** is able to assemble into discrete cyclic rosettes, while **2** tends to form polymeric hydrogen-bonded tapes, which further assemble into an extended 3D structure. We assume that a morphological mismatch between the assemblies of **2** and PC<sub>61</sub>BM might be responsible for the observed macroscopic phase separation, which should render **2** unfavorable for photovoltaic applications.

Reflecting the significant difference in the phase separation, **1**:PC<sub>61</sub>BM and **2**:PC<sub>61</sub>BM show distinct difference in the photovoltaic property of their solution-processed BHJ solar cells. The devices were fabricated using

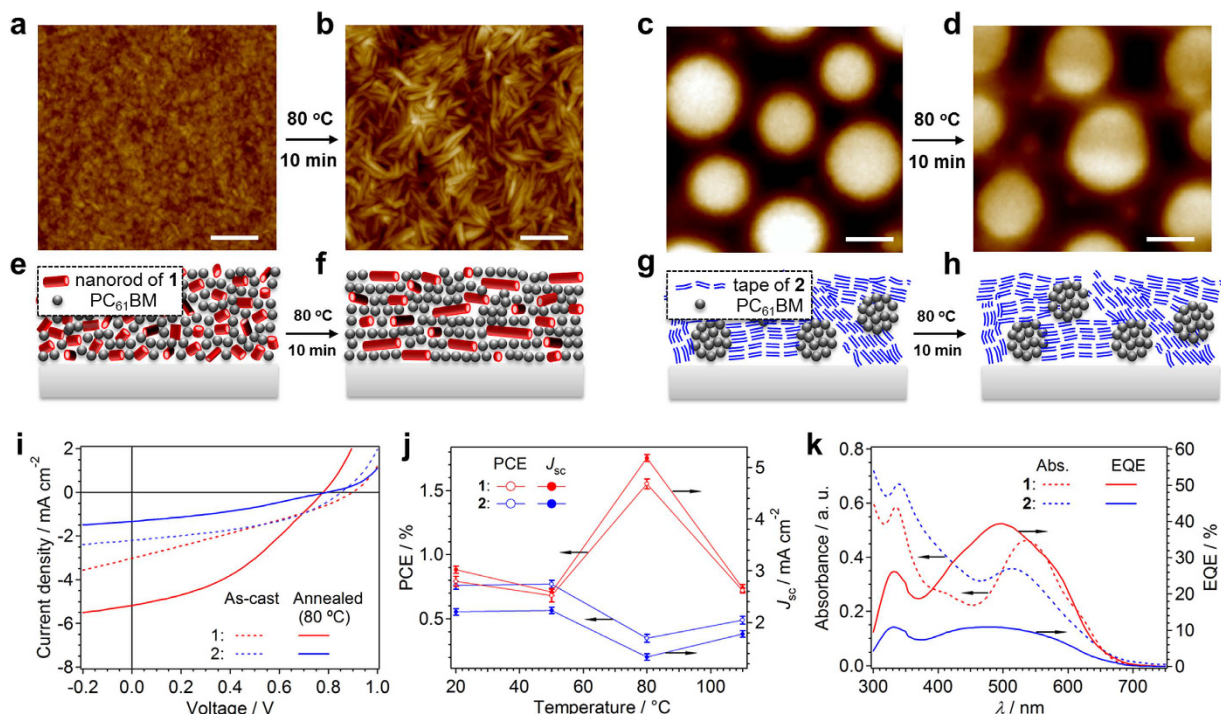


**Figure 6. Morphology and photovoltaic properties of p-n heterojunction structures.** (a–d) AFM images of as-cast (a,c) and annealed (b,d) thin films of 1:PC<sub>61</sub>BM (a,b) and 2:PC<sub>61</sub>BM (c,d); scale bar, 200 nm. Thin film samples were prepared by spin-coating CHCl<sub>3</sub> solutions of 1:PC<sub>61</sub>BM and 2:PC<sub>61</sub>BM ( $c_{\text{total}} = 20 \text{ mg mL}^{-1}$ ) onto substrates. Annealing conditions:  $T = 80 \text{ }^\circ\text{C}$ ,  $t = 10 \text{ min}$ . (e–h) Schematic illustration of morphological change of 1:PC<sub>61</sub>BM (e,f) and 2:PC<sub>61</sub>BM (g,h) upon annealing. (i) Current–voltage ( $J$ – $V$ ) characteristics of BHJ solar cells using 1:1 (w:w) blend films of 1:PC<sub>61</sub>BM (red lines) and 2:PC<sub>61</sub>BM (blue lines) before (dotted lines) and after annealing at  $80 \text{ }^\circ\text{C}$  (solid lines). (j) PCE and  $J_{\text{sc}}$  values of devices containing 1 (red) and 2 (blue) as a function of the annealing temperature. (k) UV-vis absorption (dashed curves) and EQE spectra (solid curves) of thermally annealed ( $T = 80 \text{ }^\circ\text{C}$ ) 1:1 (w:w) blend films of 1:PC<sub>61</sub>BM (red) and 2:PC<sub>61</sub>BM (blue). Film thickness: 100–120 nm. Average values of four cells with standard deviation.

as-cast blend films, as well as that were thermally annealed at 50, 80, and  $110 \text{ }^\circ\text{C}$ . As **1** and **2** have almost identical optical and electrochemical properties (Fig. 6k and see Supplementary Table S1) as well as comparable hole mobilities in the orders of  $10^{-4}$ – $10^{-5} \text{ cm}^2 \text{ V}^{-1} \text{ s}^{-1}$  (see Supplementary Table S2), the photovoltaic performance of their solar cells should depend strongly on their supramolecular structures<sup>58</sup>. The device performance of **1** and **2** exhibited a diametral bell-shaped dependency on the annealing temperature although the devices with as-cast films showed comparable power conversion efficiency (PCE) of 0.8% and short-circuit current density ( $J_{\text{sc}}$ ) values (Fig. 6i,j). Devices using **1** showed a notable performance increase upon annealing at  $80 \text{ }^\circ\text{C}$  (PCE:  $0.8 \rightarrow 1.5\%$ ), while those using **2** showed a substantially diminished performance (PCE: from  $0.8 \rightarrow 0.3\%$ ). As the open-circuit voltage values ( $V_{\text{oc}}$ ) of all devices were observed consistently at  $0.8$ – $0.9 \text{ V}$  (see Supplementary Table S3), the annealing-dependence of the PCE may be directly associated with the variation of the  $J_{\text{sc}}$  values, which could in turn be correlated with the distinctive difference in the degree of phase separation because of comparable hole mobilities of **1** and **2**. The BHJ films of **1** and **2** annealed at  $80 \text{ }^\circ\text{C}$  showed a large difference in external quantum efficiency (EQE; **1**: 39.4% at 520 nm; **2**: 10.9% at 510 nm), albeit that only a small difference in their absorption band (300–600 nm) was observed (Fig. 6k). This finding revealed a substantially more efficient photoelectron conversion in the BHJ films of **1** relative to those of **2**. As expected, such a distinct device performance was not observed for devices based on the non-aggregating  $N,N'$ -dimethylated derivatives **1-Me** and **2-Me**. For BHJ films of these non-aggregative compounds, no significant morphology change was observed upon thermal annealing (Supplementary Fig. 21), and the PCE values of the devices did not exceed 1%, even after thermal annealing (see Supplementary Table S4). Similar relation between the phase-separated structure and the device performance as observed between **1** and **2** have been well documented for P3HT/PC<sub>61</sub>BM systems<sup>59</sup>, wherein degrees of phase-separation can be controlled physically through solution processing. In the present study the phase-separation could be controlled by means of a supramolecular approach that guarantee high-fidelity self-assembly pathways expanding from the molecular to the bulk level.

## Conclusion

Our experimental data demonstrate that even minor structural alterations in self-assembling building blocks are able to fully control their self-assembly pathways on all levels of hierarchy. This high-fidelity control over self-assembly pathways arises from directional hydrogen-bonding interactions, which render rerouting to other

self-assembly pathways difficult. The absence of long aliphatic chains, which are widely used to increase the solubility of functional supramolecular building blocks, is an important factor in our molecular design, as their bulk, flexibility, and van der Waals interactions decisively control the stable self-assembled architectures observed under the conditions applied. Instead of long aliphatic chains, we grafted short alkyl chains onto the  $\pi$ -conjugated backbone in order to embed them within the resulting assemblies, which should ensure good solubility without decisively impacting the self-assembled architectures. It should be possible to apply a similar molecular design concept to a variety of other functional molecules, and therefore, we believe that our study expands the scope of controlling self-assembly pathways to obtain specific self-assembled materials including several levels of hierarchy.

## Materials and Methods

The PC<sub>61</sub>MB was purchased from Wako Chemicals (Wako Pure Chemical Industries, Ltd.). The rest of chemical reagents were purchased from TCI Chemicals (Tokyo Chemical Industry Co., Ltd.) and used without further purification. Column chromatography was performed using 63–210  $\mu$ m silica gel. The solvents for the preparation of assemblies were all spectral grade and used without further purification. <sup>1</sup>H and <sup>13</sup>C NMR spectra were recorded on Bruker DPS300 and JEOL JNM-ECA500 NMR spectrometers and chemical shifts are reported in ppm ( $\delta$ ) with the signal of TMS as internal standard. ESI-MS spectra were measured on an Exactive (Thermo Scientific). UV/Vis spectra were recorded on a JASCO V660 spectrophotometer. Differential scanning calorimetry was performed on SII DSC6220. Molecular mechanics calculations were performed on MacroModel version 10.4 using AMBER\* force field.

**Vapor pressure osmometry (VPO).** Vapor pressure osmometry analysis was performed using KNAUER Vapor Pressure Osmometer K-7000 with EuroOsmo 7000 software. CHCl<sub>3</sub> was used as solvent for measurements and the temperature for measurements was 25 °C. Benzil was used as a standard for calibration. Sample and standard solutions were prepared by dissolving each compound in CHCl<sub>3</sub> to achieve a target concentration of 10, 20, 50 or 100 mM. Before performing all sample measurements, the reference condition was established by attaching pure CHCl<sub>3</sub> on both thermistors and performing AUTOZERO. Solutions of the standard and samples at identical concentrations were entered for every single run and at least three osmograms were recorded for a given concentration. Droplets of pure CHCl<sub>3</sub> and sample solutions were placed on separate thermistors surrounded by pure solvent vapor. Thermistors were washed after every measurement in order to avoid the contamination by solutions of different concentrations. The size of each drop was kept as constant as possible and equal on both thermistors. In order to keep saturated atmosphere around the thermistors, the chamber was equipped with specially shaped filter papers. The difference in vapor pressures between the two droplets was detected as the difference in temperature at each thermistor. The calibration curve was prepared by measuring CHCl<sub>3</sub> solutions of benzil. EuroOsmo software was used to draw the graphs and to calculate the calibration constant and molecular weights. Because VPO apparatus is a sensitive piece of equipment, measurement of each concentration was repeated four times to confirm the accuracy of the recorded data.

**DOSY experiments.** Sample solutions were prepared by dissolving each compound in CDCl<sub>3</sub> to achieve a target concentration of 1, 5, 10, 20 or 100 mM. All the solutions were warmed at 60 °C for 10 min in a vial to ensure complete dissolution of the compounds, and equilibrated at room temperature at least 30 min before the measurement. Each solution was transferred to a micro NMR tube with the glass magnetic susceptibility matched to chloroform (Shigemi, BMS-005J). The solution height was adjusted to be 10 mm in the 5 mm O.D. tube. The spectra were recorded on a JEOL JNM-ECX400 spectrometer at the resonance frequency of 399.7822 MHz for <sup>1</sup>H. The temperature was regulated at 25 °C and no spin was applied during measurements. All the experiments were performed using the bipolar pulse longitudinal eddy current delay (BPP-LED) sequence with spoil gradients applied during the diffusion and eddy current decay periods. The gradient duration was 1 ms and the diffusion time was within the range of 80–100 ms. The gradient strength was varied at even interval on a log-2 scale from 3 to 270 mT m<sup>-1</sup> in 14 steps. DOSY spectra were generated by the JEOL's native program Delta, using the adapted CONTIN algorithm for inverse Laplace transforms to build the diffusion dimension.

**Scanning Tunneling Microscopy (STM).** Each compound was dissolved in 1-phenyloctane, (S)- or (R)-limonene ( $c < 1 \times 10^{-4}$  M). A drop of these solutions was placed on a freshly cleaved highly ordered pyrolytic graphite (HOPG) to prepare a monolayer at the liquid-solid interface. Low current STM observation was performed using a Nanoscope IIIa system (Digital Instruments, Santa Barbara, CA) at freshly cleaved HOPG/solvent interface. STM tips were mechanically cut and sharpened from Pt/Ir wire (90/10). The STM imaging conditions (current and bias voltage) are given in each figure caption. All the STM images were recorded in the constant current mode, and analyzed by the SPIP software (Image Metrology, Denmark).

**Synchrotron radiation X-ray diffraction experiments.** Powder X-ray diffraction (PXRD) patterns of the bulk samples and grazing incidence X-ray diffraction (GI-XRD) images of the film samples were obtained using the BL45XU beamline at SPring-8 (Hyogo, Japan) equipped with an R-Axis IV++ (Rigaku) imaging plate area detector or with a Pilatus 3  $\times$  2 M (Dectris) detector. The scattering vector,  $q = 4\pi\sin\theta/\lambda$ , and the position of incident X-ray beam on the detector were calibrated using several orders of layer reflections from silver behenate ( $d = 58.380$  Å), where  $2\theta$  and  $\lambda$  refer to the scattering angle and wavelength of the X-ray beam (1.00 Å), respectively. The sample-to-detector distances for PXRD and GI-XRD measurements were 0.40 and 0.38 m, respectively. The obtained diffraction patterns and images were integrated along the Debye-Scherrer ring to afford one-dimensional intensity data using the FIT2D software (<http://www.esrf.eu/computing/scientific/FIT2D/>). The lattice parameters were refined using the CellCalc ver. 2.10 software ([http://homepage2.nifty.com/~hsc/soft/cellcalc\\_e.html](http://homepage2.nifty.com/~hsc/soft/cellcalc_e.html)).

**Atomic force microscopy (AFM).** AFM images were acquired under ambient conditions using Multimode 8 Nanoscope V (Bruker Instruments) in Tapping mode or Peak Force Tapping (Scanasynt) mode. Silicon cantilevers (MPP-21100-10) with a spring constant of 3 N/m and frequency of 70 kHz (nominal value, Bruker, Japan) or silicon cantilevers (SCANASYST-AIR) with a spring constant of 0.4 N/m and frequency of 70 kHz (nominal value, Bruker, Japan) were used for Tapping mode and Scanasynt mode, respectively. Samples were prepared by spin-coating assembly solutions onto a freshly cleaved highly-oriented pyrolytic graphite (HOPG).

**Photovoltaic devices.** Bulk heterojunction solar cell devices were fabricated on indium-tin oxide (ITO) coated glass with a device structure Al/Ca/BHJ film/PEDOT:PSS/ITO. The ITO was cleaned with acetone and 2-propanol in ultrasonic bath. The resultant ITO substrates were exposed to UV-ozone for 20 min and then coated with PEDOT:PSS [poly(3,4-ethylene dioxythiophene):poly(styrene sulfonate)] (thickness: ca. 30 nm). The substrates were heated for 20 min at 120 °C to remove residual water. In a N<sub>2</sub> glove box, 0.5 mL of chloroform solutions containing PC<sub>61</sub>BM (5 mg, Luminescence Technology Corp., Taiwan Province) and donor materials (5 mg) were spin-coated (1000 rpm for 30 sec) onto the substrate. The thickness of the resulting BHJ films (100–120 nm) was determined by using a DEKTAK surface profiler (Bruker AXS). The substrates were then moved to a high-vacuum chamber, and the top electrode was evaporated through a shadow mask (Ca:10 nm, Al:90 nm) to give solar cells with an active area of 0.04 cm<sup>2</sup>. Finally, the devices were encapsulated by a glass lid in the nitrogen glove box system. The *J*-*V* characteristics of the solar cells were evaluated by using a Keithley 2400 source-measure unit. The AM 1.5 G light was provided by a filtered Xe lamp. The intensity of 100 mW cm<sup>-2</sup> of the AM 1.5 G light was determined by using a calibrated inorganic solar cell from the National Institute of Advanced Industrial Science and Technology (Japan). No spectral mismatch factor was included in the calculation of the efficiency.

**Hole mobility measurements.** Hole mobilities of **1** and **2** films (prepared from 10-mg/ml CHCl<sub>3</sub> solutions) were estimated by charge-only space-charge limited current (SCLC) method. The SCLC is described by  $J = 9\epsilon_0\epsilon_r\mu V^2/8L^3$ , where *J* is the current density, *L* is the film thickness of the active layer,  $\mu$  is the hole mobility,  $\epsilon_r$  is the relative dielectric constant of the transport medium,  $\epsilon_0$  is the permittivity of free space ( $8.85 \times 10^{-12}$  F m<sup>-1</sup>), *V* is the applied voltage to the device. SCLC measurements were carried out with a device structure of ITO/PEDOT:PSS/active layer/MoO<sub>3</sub>/Al by taking the current density in the range 0–10 V and fitting the results to a space-charge limited form.

## References

1. Schenning, A. P. H. J. & Meijer, E. W. Supramolecular electronics; nanowires from self-assembled  $\pi$ -conjugated systems. *Chem. Commun.* 3245–3258 (2005).
2. Jain, A. & George, S. J. New directions in supramolecular electronics. *Mater. Today* **18**, 206–214 (2015).
3. Korevaar, P. A. *et al.* Pathway complexity in supramolecular polymerization. *Nature* **481**, 492–496 (2012).
4. Ogi, S., Sugiyasu, K., Manna, S., Samitsu, S. & Takeuchi, M. Living supramolecular polymerization realized through a biomimetic approach. *Nat. Chem.* **6**, 188–195 (2014).
5. Yamauchi, M., Ohba, T., Karatsu, T. & Yagai, S. Photoreactive helical nanoaggregates exhibiting morphology transition on thermal reconstruction. *Nat. Commun.* **6**, 8936–8972 (2015).
6. Ogi, S., Stepanenko, V., Thein, J. & Würthner, F. Impact of alkyl spacer length on aggregation pathways in kinetically controlled supramolecular polymerization. *J. Am. Chem. Soc.* **138**, 670–678 (2016).
7. Mukhopadhyay, R. D. & Ajayaghosh, A. Living supramolecular polymerization. *Science* **349**, 241–242 (2015).
8. Jonkheijm, P. *et al.* Transfer of  $\pi$ -conjugated columnar stacks from solution to surfaces. *J. Am. Chem. Soc.* **125**, 15941–15949 (2003).
9. Yagai, S. *et al.* Diversification of self-organized architectures in supramolecular dye assemblies. *J. Am. Chem. Soc.* **129**, 13277–13287 (2007).
10. Rosen, B. M. *et al.* Dendron-mediated self-assembly, disassembly, and self-organization of complex systems. *Chem. Rev.* **109**, 6275–6540 (2009).
11. Babu, S. S., Prasanthkumar, S. & Ajayaghosh, A. Self-assembled gels for organic electronics. *Angew. Chem. Int. Ed.* **51**, 1766–1776 (2012).
12. Ghosh, S., Praveen, V. K. & Ajayaghosh, A. The chemistry and applications of  $\pi$ -gels. *Annu. Rev. Mater. Res.* **46**, 235–262 (2016).
13. Korevaar, P. A., Newcomb, C. J., Meijer, E. W. & Stupp, S. I. Pathway selection in peptide amphiphile assembly. *J. Am. Chem. Soc.* **136**, 8540–8543 (2014).
14. Yagai, S. *et al.* Design amphiphilic dipolar  $\pi$ -systems for stimuli-responsive luminescent materials using metastable states. *Nat. Commun.* **5**, 4013–4022 (2014).
15. Aliprandi, A., Mauro, M. & De Cola, L. Controlling and imaging biomimetic self-assembly. *Nat. Chem.* **8**, 10–15 (2016).
16. Tschierske, C. Non-conventional liquid crystals: the importance of micro-segregation for self-organization. *J. Mater. Chem.* **8**, 1485–1508 (1998).
17. Yagai, S. *et al.* Supramolecular polymerization and polymorphs of oligo(p-phenylene vinylene)-functionalized bis- and monoureas. *Chem. Eur. J.* **14**, 5426–5257 (2008).
18. An, B.-K. *et al.* Strongly fluorescent organogel system comprising fibrillar self-assembly of a trifluoromethyl-based cyanostilbene derivative. *J. Am. Chem. Soc.* **126**, 10232–10233 (2004).
19. Xie, Z., Stepanenko, V., Fimmel, B. & Würthner, F. An organogelator design without solubilizing side chains by backbone contortion of a perylene bisimide pigment. *Mater. Horiz.* **1**, 355–359 (2014).
20. Yagai, S. *et al.* Supramolecular engineering of oligothiophene nanorods without insulators: hierarchical association of rosettes and photovoltaic properties. *Chem. Eur. J.* **20**, 16128–16137 (2014).
21. Zimmerman, S. C., Zeng, F., Reichert, D. E. C. & Kolotuchin, S. V. Self-assembling dendrimers. *Science* **271**, 1095–1098 (1996).
22. Kato, T. Self-assembly of phase-segregated liquid crystal structures. *Science* **295**, 2414–2418 (2002).
23. Yagai, S. *et al.* Supramolecularly engineered perylene bisimide assemblies exhibiting thermal transition from columnar to multilamellar structures. *J. Am. Chem. Soc.* **134**, 7983–7994 (2012).
24. Dordevic, L. *et al.* Solvent molding of organic morphologies made of supramolecular chiral polymers. *J. Am. Chem. Soc.* **137**, 8150–8160 (2015).
25. Henze, O. *et al.* Chiral Amphiphilic Self-Assembled  $\alpha,\alpha'$ -Linked Quinque-, Sexi-, and Septithiophenes: Synthesis, Stability and Odd-Even Effects. *J. Am. Chem. Soc.* **128**, 5923–5929 (2006).
26. Pieraccini, S. *et al.* Solvent-induced switching between two supramolecular assemblies of a guanosine-terthiophene conjugate. *Org. Biomol. Chem.* **8**, 774–781 (2010).

27. Di Maria, F. *et al.* A Successful Chemical Strategy To Induce Oligothiophene Self-Assembly into Fibers with Tunable Shape and Function. *J. Am. Chem. Soc.* **133**, 8654–8661 (2011).
28. Klingstedt, T. *et al.* The Structural Basis for Optimal Performance of Oligothiophene-Based Fluorescent Amyloid Ligands: Conformational Flexibility is Essential for Spectral Assignment of a Diversity of Protein Aggregates. *Chem. Eur. J.* **19**, 10179–10192 (2013).
29. Zerkowski, J. A., Seto, C. T. & Whitesides, G. M. Solid-state structures of “rosette” and “crinkled tape” motifs derived from the cyanuric acid-melamine lattice. *J. Am. Chem. Soc.* **114**, 5473–5475 (1992).
30. Bielejewska, A. G. *et al.* Thermodynamic stabilities of linear and crinkled tapes and cyclic rosettes in melamine-cyanurate assemblies: a model description. *J. Am. Chem. Soc.* **123**, 7518–7533 (2001).
31. Seto, C. T., Mathias, J. P. & Whitesides, G. M. Molecular self-assembly through hydrogen bonding: aggregation of five molecules to form a discrete supramolecular structure. *J. Am. Chem. Soc.* **115**, 1321–1329 (1993).
32. Higler, I. *et al.* Stable heterotopic noncovalent resorcin[4]arene assemblies. *Eur. J. Org. Chem.* 1727–1734 (2000).
33. Yagai, S., Iwai, K., Karatsu, T. & Kitamura, A. Photoswitchable exciton coupling in merocyanine–diarylethene multi-chromophore hydrogen-bonded complexes. *Angew. Chem. Int. Ed.* **51**, 9679–9683 (2012).
34. Jiao, T. & Liu, M. Supramolecular Assemblies and Molecular Recognition of Amphiphilic Schiff Bases with Barbituric Acid in Organized Molecular Films. *J. Phys. Chem. B* **109**, 2532–2539 (2005).
35. Martin, R. B. Comparisons of indefinite self-association models. *Chem. Rev.* **96**, 3043–3064 (1996).
36. Goldstein, R. F. & Stryer, L. Cooperative polymerization reactions. *Biophys. J.* **50**, 583–599 (1986).
37. Smulders, M. M. J. *et al.* How to distinguish isodesmic from cooperative supramolecular polymerization. *Chem. Eur. J.* **16**, 362–367 (2010).
38. Jonkheijm, P., van der Schoot, P., Schenning, A. P. H. J. & Meijer, E. W. Probing the solvent-assisted nucleation pathway in chemical self-assembly. *Science* **313**, 80–83 (2006).
39. Montoro-Garcia, C. *et al.* High-fidelity noncovalent synthesis of hydrogen-bonded macrocyclic assemblies. *Angew. Chem. Int. Ed.* **54**, 6780–6784 (2015).
40. Miura, A. *et al.* 2D self-assembly of oligo(p-phenylene vinylene) derivatives: from dimers to chiral rosettes. *Small* **1**, 131–137 (2005).
41. De Cat, I. *et al.* Induction of chirality in an achiral monolayer at the liquid/solid interface by a supramolecular chiral auxiliary. *J. Am. Chem. Soc.* **134**, 3171–3177 (2012).
42. Chen, T., Wang, D. & Wan, L.-J. Two-dimensional chiral molecular assembly on solid surfaces: formation and regulation. *National Science Review* **2**, 205–216 (2015).
43. Elemans, J. A., De Cat, I., Xu, H. & De Feyter, S. Two-dimensional chirality at liquid–solid interfaces. *Chem. Soc. Rev.* **38**, 722–736 (2009).
44. Aimi, J., Oya, K., Tsuda, A. & Aida, T. Chiroptical sensing of asymmetric hydrocarbons using a homochiral supramolecular box from a bismetalporphyrin rotamer. *Angew. Chem. Int. Ed.* **46**, 2031–2035 (2007).
45. Stepanenko, V., Li, X.-Q., Gershberg, J. & Würthner, F. Evidence for kinetic nucleation in helical nanofiber formation directed by chiral solvent for a perylene bisimide organogelator. *Chem. Eur. J.* **19**, 4176–4183 (2013).
46. Katsonis, N. *et al.* Emerging solvent-induced homochirality by the confinement of achiral molecules against a solid surface. *Angew. Chem. Int. Ed.* **47**, 4997–5001 (2008).
47. Yagai, S. *et al.* Supramolecularly engineered aggregation of a dipolar dye: vesicular and ribbonlike architectures. *Angew. Chem. Int. Ed.* **49**, 9990–9994 (2010).
48. Chu, C.-C. *et al.* Self-assembly of supramolecular fullerene ribbons via hydrogen-bonding interactions and their impact on fullerene electronic interactions and charge carrier mobility. *J. Am. Chem. Soc.* **132**, 12717–12723 (2010).
49. Ahn, S. & Matzger, A. J. Six different assemblies from one building block: two-dimensional crystallization of an amide amphiphile. *J. Am. Chem. Soc.* **132**, 11364–11371 (2010).
50. Tahara, K., Lei, S., Adisojoso, J., De Feyter, S. & Tobe, Y. Supramolecular surface-confined architectures created by self-assembly of triangular phenylene-ethynylene macrocycles via van der Waals interaction. *Chem. Commun.* 8507–8525 (2010).
51. Ghiviriga, I. & Oniciu, D. C. Steric hindrance to the solvation of melamines and consequences for non-covalent synthesis. *Chem. Commun.* 2718–2719 (2002).
52. Yagai, S. *et al.* Reversible transformation between rings and coils in a dynamic hydrogen-bonded self-assembly. *J. Am. Chem. Soc.* **131**, 5408–5410 (2009).
53. Yagai, S. *et al.* Interconvertible oligothiophene nanorods and nanotapes with high charge-carrier mobilities. *Chem. Eur. J.* **15**, 9320–9324 (2009).
54. Yagai, S., Goto, Y., Karatsu, T., Kitamura, A. & Kikkawa, Y. Catenation of self-assembled nanorings. *Chem. Eur. J.* **17**, 13657–13660 (2011).
55. Yagai, S. *et al.* Self-organization of hydrogen-bonding naphthalene chromophores into J-type nanorings and H-type nanorods: impact of regioisomerism. *Angew. Chem. Int. Ed.* **51**, 6643–6647 (2012).
56. Heeger, A. J. 25th anniversary article: bulk heterojunction solar cells: understanding the mechanism of operation. *Adv. Mater.* **26**, 10–27 (2014).
57. Mishra, A. & Bäuerle, P. Small Molecule Organic Semiconductors on the Move: Promises for Future Solar Energy Technology. *Angew. Chem. Int. Ed.* **51**, 2020–2067 (2012).
58. Würthner, F. & Meerholz, K. Systems chemistry approach in organic photovoltaics. *Chem. Eur. J.* **16**, 9366–9373 (2010).
59. Li, T. *et al.* High-efficiency solution processable polymer photovoltaic cells by self-organization of polymer blends. *Nat. Mater.* **4**, 864–868 (2005).

## Acknowledgements

This work was supported by KAKENHI (no. 26102010), a Grant-in-Aid for Scientific Research on Innovative Areas “ $\pi$ -Figuration” (no. 26102001) of The Ministry of Education, Culture, Sports, Science, and Technology, Japan. The part of solar cell devices was supported by CREST, JST. Synchrotron XRD experiments were carried out at the BL45XU beamline of SPring-8, with the approval of the RIKEN SPring-8 Center (proposal nos 20140056 and 20150068). The authors would like to thank Dr. Bimalendu Adhikari and Dr. Deepak D. Prabhu for helpful discussions.

## Author Contributions

S.Y. and X.L. conceived the project and contributed to the concept of the manuscript. M.S., M.G., and X.L. synthesized and characterized the compounds, and performed experimental works on self-assembly. M.S. and H.Y. performed the NMR experiments. Y.K. performed the STM experiments. M.Y., T. Kajitani, and T.F. performed the XRD experiments and analyzed the XRD results. T. Kizaki, Y.T., and K.N. completed the photovoltaic devices fabrication and performance evaluation. S.Y. and X.L. wrote the manuscript. T. Karatsu discussed the results and commented on the manuscript.

## Additional Information

**Supplementary information** accompanies this paper at <http://www.nature.com/srep>

**Competing financial interests:** The authors declare no competing financial interests.

**How to cite this article:** Lin, X. *et al.* High-fidelity self-assembly pathways for hydrogen-bonding molecular semiconductors. *Sci. Rep.* 7, 43098; doi: 10.1038/srep43098 (2017).

**Publisher's note:** Springer Nature remains neutral with regard to jurisdictional claims in published maps and institutional affiliations.



This work is licensed under a Creative Commons Attribution 4.0 International License. The images or other third party material in this article are included in the article's Creative Commons license, unless indicated otherwise in the credit line; if the material is not included under the Creative Commons license, users will need to obtain permission from the license holder to reproduce the material. To view a copy of this license, visit <http://creativecommons.org/licenses/by/4.0/>

© The Author(s) 2017